UNIVERSITY
OF TRENTO

DEPARTMENT OF INFORMATION AND COMMUNICATION TECHNOLOGY

38050 Povo – Trento (Italy), Via Sommarive 14
http://www.dit.unitn.it

MORPHOLOGICAL PROCESSING OF ELECTROMAGNETIC SCATTERING DATA FOR ENHANCING THE RECONSTRUCTION ACCURACY OF THE ITERATIVE MULTI-SCALING APPROACH

D. Franceschini, A. Rosani, M. Donelli, M. Pastorino, and A. Massa

March 2008

Technical Report <u>DISI 08-016</u>

Morphological Processing of Electromagnetic Scattering Data for Enhancing the Reconstruction Accuracy of the Iterative Multi-Scaling Approach

Davide Franceschini[1], Andrea Rosani[1], Massimo Donelli[1],
Matteo Pastorino[2], and Andrea Massa[1]

[1] ELEDIA - Department of Information and Communication Technology, University of Trento
Via Sommarive 14, I-38050 Trento, Italy
Phone: +39 0461 882057, Fax: +39 0461 882093, E-mail: *andrea.massa@ing.unitn.it*

[2] DIBE - Biophysical and Electronic Engineering Department, University of Genoa
Via Opera Pia 11A, 16145 Genoa, Italy
Phone: +39 010 3532242, Fax: +39 0103532245, E-mail: *pastorino@dibe.unige.it*

Abstract − This work is aimed at presenting a methodology that exploits the scattered electromagnetic radiation collected on a measurement region outside the area under investigation to locate and characterize multiple unknown profiles. In many practical cases, an accurate quantitative imaging of the scenario under test is required and it can be reached by using a high resolution representation of the dielectric profile of the scatterers. Towards this aim, an enhanced iterative multi-resolution procedure that exploits a morphological processing for detecting and focusing on different non-connected regions-of-interest is developed.
A suitable set of representative numerical results is presented for demonstrating that the proposed approach is able to efficiently detect the objects located in the test domain and to enhance the accuracy in reconstructing multiple scatterers

Keywords − Microwave Imaging, Inverse Scattering, Multiresolution Reconstruction, Morphological Operators

I.   INTRODUCTION

Microwave imaging techniques are based on the numerical processing of the scattered electromagnetic radiation collected on a measurement domain lying outside the region under test. Such methodologies find a variety of applications in biomedical sciences (e.g., breast cancer imaging [1]), in the context of the subsurface inspection [2] and of the non-destructive industrial testing [3].

However, whatever the application, the information content of the problem data turns out to be intrinsically bounded [4] and thus an high-resolution and uniform quantitative imaging of the scenario under test cannot be realized by simply processing the scattered data and without proper countermeasures. On the other hand, every practical application requires the representation of the dielectric or conductivity profiles (i.e., discontinuities with respect to the background medium) with a detailed level of spatial resolution.

In order to address such issues, different kinds of multiresolution approaches have been proposed [5]-[9] in order to meet the accuracy requirements although in the presence of a limited amount of informative data. These techniques avoid a fine and homogeneous discretization in the whole investigation domain by properly employing a high resolution level only in some regions-of-interest (RoIs) belonging to the area under test.

Pursuing this idea, *Miller et al.* [5][6] proposed statistically-based approaches, while other works introduced a wavelet expansion [7][8] of the unknowns in the test domain. Successively, the Iterative Multi-Scaling Algorithm (IMSA) has been presented in [9]. Such a methodology iteratively reconstructs an unknown scenario exploiting an adaptive allocation of the resolution levels according to the information gained during a multi-step retrieval process. Therefore, an enhanced resolution in the regions-of-interest is guaranteed, since the data collected through the field measurement are efficiently exploited and new information on the scenario is acquired during the multi-step procedure. Notwithstanding the effectiveness of the IMSA in many situations and conditions [9], it presented some limitations in dealing with multiple-scatterers configurations. Thus, the integration of a suitable procedure able to localize multiple objects in a search domain was mandatory. Certainly, many different approaches could be, in principle, integrated in the IMSA, as for example the method of decomposition of the time reversal operator (DORT) [10] or the level set method (LSM) [11]. The former allows to locate a set of unknown scatterers with a reduced sensitivity to the noise, but the sizes of the scatterers have to be smaller than half a wavelength and the objects should be separated by more than a third of a wavelength. The LSM is also very effective in determining the location and the

shape of unknown obstacles but it requires the knowledge of the dielectric parameters of the scatterers under test. Moreover, a technique for finding the minimum circular envelope enclosing a set of scatterers and successively localize them has been proposed in [12]. Even though it avoids the solution of the full inverse problem, such an approach cannot provide any estimation of the extension of the RoIs.

However, in several applications a quantitative characterization of the dielectric properties of multiple RoIs is required and the localization or the shaping of the scatterers is not enough. For such a reason an improved version of the IMSA has been proposed in [13] by integrating a clustering procedure [13] between successive steps of the multi-scaling algorithm. The numerical and the experimental assessment have demonstrated the accuracy of the approach in resolving different non-connected regions-of-interest exploiting a suitable processing of intermediate reconstructions. The pixel representation of the retrieved profile is firstly binarized by thresholding the arising image according to the histogram analysis. Successively, a scanning of the image allows the detection and the definition of the RoIs where the scatterers are supposed to be located and where the resolution level will be increased. Unfortunately, such a procedure presents some deficiencies since the arising reconstruction accuracy turns out to be dependent in a significant fashion on the thresholding process in the histogram analysis. Therefore, a new set of morphological transformations [14][15] has been developed and integrated in the multi-scaling algorithm in order to substitute the clustering procedure [13] and allow a more detailed detection of the RoIs without a large increase in the overall computational burden.

This paper will be structured as follows. In Sect. II, the mathematical formulation of the morphological processing for the RoIs definition and its integration in the IMSA will be presented. In Sect. III, a comparative analysis will be carried out in order to assess the advantages and the robustness of the proposed approach [called morphological IMSA, (M-IMSA)] in dealing with a selected set of representative scattering configurations. Eventually, some conclusions are drawn (Sect. IV).

II. PROBLEM FORMULATION

The two-dimensional geometry of Fig. 1 showing a cross sectional view of an inhomogeneous investigation domain D_I will be considered in the following. Such a scenario is sensed through a set of monochromatic incident electric fields TM polarized impinging from V different directions [$E_v^{inc}(x,y)\hat{\underline{z}}$, $v = 1,...,V$].

The properties of the dielectric profile under test are modeled by means of the object function $\tau(x,y)$

$$\tau(x,y) = \varepsilon_r - 1 - j\frac{\sigma(x,y)}{\omega\varepsilon_0} \tag{1}$$

where ε_r and σ denote the relative permittivity and the conductivity, respectively.

The measures of the scattered field ($E_v^{scatt}(x_m,y_m)\hat{\underline{z}}$, $v = 1,...,V$) are collected at $m = 1,...,M$ positions belonging to the measurement domain D_O located outside D_I. These data are related to the contrast function $\tau(x,y)$ by means of the well-known integral equations [16]

$$E_v^{scatt}(x_m,y_m) = S_v^{ext}\left[\tau(x_n,y_n),E_v^{tot}(x_n,y_n)\right] \tag{2}$$

$$E_v^{inc}(x_n,y_n) = E_v^{tot}(x_n,y_n) - S_v^{int}\left[\tau(x_n,y_n),E_v^{tot}(x_n,y_n)\right] \tag{3}$$

where the external and internal scattering operators [16] are denoted by $S_v^{ext}[\cdot]$ and $S_v^{int}[\cdot]$, respectively; $\tau(x_n,y_n)$ and $E_v^{tot}(x_n,y_n)$, $n = 1,...,N$, are the unknowns whose N-dimensional finite representation has to be reconstructed by solving a non-linear and ill-posed problem.

Moreover, an efficient allocation of the unknowns and thus a suitable discretization of the Regions-of-Interests (RoIs) of D_I are necessary for a reliable processing of the limited amount of information collectable from the field measures.

Towards this purpose, the M-IMSA aims at defining, through a multi-step ($s = 1,...,S_{opt}$) procedure, a multiresolution reconstruction of the unknown domain under test according to the flow-chart in Fig. 2, where the sequence of the main M-IMSA operations and the integrated morphological processing are sketched. In more detail, the structure of the algorithm can be described by considering four macro-blocks: the *Profile Retrieval* stage, the *Profile Processing* stage, the *Convergence Check,* and the block responsible for the definition of the resolution level in the RoIs.

A. Profile Retrieval

After the initialization of the unknowns to the free-space configuration, the number of RoIs is set to $I^{(0)} = 1$ and $D_{RoI(0)}^{(1)} \equiv D_I$. Successively, the following cost function is defined

$$\Phi^{(s)} = \Phi_{Data}^{(s)} + \Phi_{State}^{(s)} \tag{4}$$

where

$$\Phi_{Data}^{(s)} = \frac{\sum_{v=1}^{V}\sum_{m=1}^{M}\left|E_v^{scatt}(x_m,y_m)-S_v^{ext}\left[\tau(x,y),E_v^{tot}(x,y)\right]\right|^2}{\sum_{v=1}^{V}\sum_{m=1}^{M}\left|E_v^{scatt}(x_m,y_m)\right|^2} \tag{5}$$

$$\Phi_{State}^{(s)} = \frac{1}{\sum_{v=1}^{V}\sum_{m=1}^{N}\left|E_v^{inc}(x_n,y_n)\right|^2}\left\{\sum_{v=1}^{V}\sum_{n=1}^{N}\left|E_v^{inc}(x_n,y_n)-\right.\right.$$
$$\left.\left. E_v^{tot}(x_n,y_n)+S_v^{int}\left[\tau(x_n,y_n),E_v^{tot}(x_n,y_n)\right]\right|^2\right\} \tag{6}$$

and minimized for determining the optimal unknowns configuration that can be related to the problem data through the scattering model defined through (2) and (3). The functional (4) can be minimized by using any available optimization tool (e.g., [17] - [19]) and the reconstructed image of the object function distribution can be processed to acquire information about the number of RoIs ($I^{(s)}$) in D_I and their extension $\left(D_{RoI(s)}^{(i)}\right)$.

B. Profile Processing

After the "*Profile Retrieval*", the retrieved image of the unknown scenario is processed with a set of morphological operations described in the following. Firstly, a *noise clipping* stage reduces the presence of the image noise thus avoiding an overestimate of the number of RoIs. Thanks to such an operation a new distribution $\tau_{nc}^{(s)}$

$$\tau_{nc}^{(s)}(x_n,y_n) = \begin{cases} 0 & if\ \tau^{(s)}(x_n,y_n)\leq\eta \\ \tau^{(s)}(x_n,y_n) & if\ \tau^{(s)}(x_n,y_n)>\eta \end{cases} \tag{7}$$

is defined, where $\eta = \mu\max\left\{\tau^{(s)}(x_n,y_n)\right\}$, μ being a parameter to be heuristically calibrated. Moreover, in order to obtain a smother distribution and to reduce the intensity of the image artifacts, the distribution $\tau_{nc}^{(s)}$ is low-pass filtered by applying a weighted average over a neighborhood ($L = 9$, L being the dimension of the neighborhood) centered around (x_n,y_n)

$$\tau_f^{(s)}(x_n,y_n) = \alpha\,\tau_{cl}^{(s)}(x_n,y_n) + \sum_{p=-1}^{1}\sum_{t=-1}^{1}\beta\,\tau_{cl}^{(s)}(x_{n+p},y_{n+t}) \tag{8}$$

with $p+t \neq 0$ and where

$$\alpha = 1 - \frac{\chi+20}{100} \tag{9}$$

$$\beta = \frac{\chi+20}{100}\frac{1}{(L-1)} \tag{10}$$

.
The filtering strength is determined by the value of the parameter χ heuristically selected during the calibration of the

thresholding stage. Successively, the RoIs are identified by firstly applying a binary transformation to $\tau_f^{(s)}$

$$\tau_T^{(s)}(x_n, y_n) = \begin{cases} 0 & \text{if } \tau_f^{(s)}(x_n, y_n) \le \kappa \\ 1 & \text{if } \tau_f^{(s)}(x_n, y_n) > \kappa \end{cases} \tag{11}$$

where $\kappa = \chi \max\{\tau_f^{(s)}(x_n, y_n)\}$, then an *erosion* of the estimated binary profiles allows to estimate the number of RoIs [$I^{(s)}$] lying in the area under test. Towards this aim, the image of $\tau_T^{(s)}$ is processed by means of a square *structuring element* Σ defined over a window of $L_\Sigma = 3 \times 3$ neighborhood pixels for defining the binary distribution $\tau_E^{(s)}$

$$\tau_E^{(s)}(x_n, y_n) = \begin{cases} 1 & \text{if } \tau_T^{(s)}(x_n, y_n) = 1 \wedge \\ & \sum_{p=-1}^{1}\sum_{t=-1}^{1} \tau_T^{(s)}(x_{n+p}, y_{n+t}) = 1 \\ 0 & \text{otherwise} \end{cases} \tag{12}$$

and in order to isolate at least one pixel (*seed*) per object in D_I. Finally, the RoI to which a seed belongs to is determined by finding the minimum square area including the subset of non-zero pixels around the considered seed.

C. Convergence Check

The block concerned with the *Profile Processing* allows the estimate of the number of RoIs, their position and their extension. By means of these informations, the convergence of the M-IMSA algorithm to a stationary reconstruction is estimated according to the stability criterion described in [13].

D. Definition of the Level of Resolution in the RoIs

If the convergence check does not hold true, the basis functions are allocated in the $I^{(s)}$ estimated RoIs according to the following rule

$$N_i^{(s)} = INT\left[\left(N^{(1)} \frac{A_i^{(s)}}{\sum_{i=1}^{I^{(s)}} A_i^{(s)}}\right)^{\frac{1}{2}}\right] \tag{13}$$

where $N_i^{(s)}$ and $A_i^{(s)}$ are the number and the area of the i-*th* region at the s-*th* step of the M-IMSA, respectively. Moreover, the function $INT[\cdot]$ provides the greater integer of its argument.

In such a way, the spatial resolution in the RoIs of D_I is increased and the accuracy of the reconstruction turns out to be further improved through the optimization of the multi-resolution version [20] of the cost function in Eq. (4).

III. NUMERICAL ANALYSIS

The aim of this Section is twofold. Firstly, some results of the analysis of the impact of the thresholding parameters on the approach performance are reported to give some indications on their optimal setting. By considering the so-defined parameter configuration, the effectiveness and robustness of the M-IMSA approach are then assessed when dealing with different scattering scenarios and conditions.

A. Calibration

As far as the morphological processing is concerned, μ and χ have to be heuristically calibrated. The first parameter is related to the noise clipping stage and it should be properly set in order to remove the image noise without compromising the reconstruction of the profile under test since an incorrect large value might significantly alter the reconstructed distribution of

the object function compared to the actual one. Moreover, the binarization stage requires the tuning of χ in order to accurately identify the RoIs. As a matter of fact, a suitable setting guarantees the detection of the number of scatterers belonging to the investigation domain without compromising the effectiveness of the proposed approach in terms of both convergence rate and computational costs.

According to these considerations a set of numerical simulations has been performed in order to define the optimal compromise between clipping effectiveness and inversion accuracy versus the values of the morphological parameters. A representative result of such a calibration is reported in Fig. 3. It concerns with the test case shown in Fig. 3(a) characterized by two $0.6\lambda_0$-sided square homogeneous dielectric ($\tau_1 = 2.0$, $\tau_2 = 0.5$) scatterers located in a square investigation area $L_{D_I} = 3.0\lambda_0$-sided. The two objects are located at ($x_o^{(1)} = y_o^{(1)} = 0.75\lambda_0$) and ($x_o^{(2)} = y_o^{(2)} = -0.6\lambda_0$). The investigation domain has been initially partitioned in $N^{(1)} = 144$ square subdomains. As far as the imaging set up is concerned, an incident plane wave impinging from $V = 8$ different equally-spaced directions has been assumed and the field measures have been collected at $M^{(v)} = 15$, $v = 1,...,V$, positions on a circular observation domain of radius $4\lambda_0$. In order to blur the scattering data, a Gaussian noise characterized by a signal-to-noise ratio (SNR) of $20dB$ has been added to the simulated field values.

For an exhaustive analysis, several simulations have been carried out varying the parameters values in the range $5 \leq \mu \leq 30$ and $10 \leq \chi \leq 35$. The results of these experiments are resumed in Fig. 3(b) where a color map of the total reconstruction error (as defined in [9]) as a function of μ and χ is reported. As it can be observed, ξ_{tot}^{M-IMSA} is lower and more stable in the regions defined by $10 \leq \mu \leq 20$ and $10 \leq \chi \leq 30$. Moreover, it reaches its minimum value in correspondence with $\mu = 20$ and $\chi = 15$ that have been assumed as optimal setting and used in the following.

B. Assessment

In this Sub-Section, a multiple object configuration will be considered in order to point out the effectiveness and the improvements allowed by the M-IMSA when compared to the standard multiple region IMSA (indicated in the following as IMSA). The imaging setup is similar to that previously described, but some geometrical parameters have been changed in order to test the effectiveness of the morphological processing in a different scenario with respect to that used in the calibration. In particular, the incident field is still a plane wave impinging from $V = 8$ different equally-spaced directions, but the field measures have been collected at $M^{(v)} = 15$ locations on a circular observation domain $2\lambda_0$ in radius. Likewise the test case in Sub-Section A, the scenario was characterized by $SNR = 20dB$.

As a first test case, let us consider the configuration shown in Fig. 4 where three $0.15\lambda_0$-sided square homogeneous dielectric ($\tau_1 = \tau_2 = 2.0$, $\tau_3 = 0.5$) scatterers are located in a square investigation area $L_{D_I} = 1.5\lambda_0$-sided at the following positions: $x_o^{(1)} = -x_o^{(2)} = -0.3\lambda_0$, $y_o^{(1)} = y_o^{(2)} = 0.525\lambda_0$, and $x_o^{(3)} = 0.0\lambda_0$, $y_o^{(3)} = -0.525\lambda_0$.

As far as the inversion results are concerned, the object function reconstructed at the first step ($s = 1$) of the M-IMSA is shown in Fig. 5(a). The set of morphological operations, described in Sect. II, have then applied to such a profile for obtaining the binary image in Fig. 5(b) where the detected RoIs are indicated.

Successively, the spatial resolution has been increased in the RoIs taking into account the discretization rule defined through Eq. (13) and the arising multi-resolution cost function has been still minimized. The result of the second step ($s = 2$) of minimization is shown in Fig. 6(a). The accuracy of the estimated contrast is improved as well as the effectiveness of the morphological operations in refining the extensions and the positions of the RoIs. Eventually, the last step of minimization provided the convergence profile ($s = S_{opt} = 3$) displayed in Fig. 6(b) where the stronger scatterers are faithfully retrieved although the estimated profile of the weak-contrast object turns out to be slightly deteriorated.

For comparison purposes, the reconstructed distribution obtained by means of the IMSA (according to the implementation proposed in [13]) is shown in Fig. 7. As it can be noticed, the M-IMSA significantly overcomes the standard IMSA since this latter is not able to detect the RoI of the weak scatterer, which is neglected from the second step onward. Quantitatively, $\xi_{tot}^{M-IMSA} = 1.53\%$ while $\xi_{tot}^{IMSA} = 2.41\%$ for the standard implementation of the IMSA. Such an event is mainly due to the high sensitivity to the noisy conditions of the clustering procedure detailed in [13]. As a matter of fact, the image histogram corresponding to the profile reconstructed at $s = 1$ is thresholded with $T_\tau = 0.7$ [13] and the RoIs detected are shown in Fig. 8. This plot points out that the support of the third object is not revealed. On the contrary, the morphological processing integrated in the iterative multi-scaling approach allows the correct detection of the actual RoIs and the retrieval of the support of the weak scatterer (Fig. 6) although it is located far from the stronger ones.

On the other hand, the behavior of the $\Phi^{(s)}$ (Fig. 9) highlights the importance from a computational point of view of an accurate estimation of the areas where the scatterers are located. As a matter of fact, the cost function of the IMSA suddenly

increases at the second step when the support of the third object is not detected and the minimization algorithm cannot retrieve a configuration of the unknowns providing a good fitting with inversion data.

Successively, a second numerical experiment has been carried out in order to assess the dependence of the M-IMSA accuracy on the distance among the objects under test. Moreover, since the morphological processing is expected to fail in distinguishing different RoIs when they are too close, the other aim of such an analysis is that of evaluating the spatial resolution capability of the M-IMSA and its reliability in comparison with that of the single-region IMSA (S-IMSA) in [9].

By referring to the scattering configuration shown in Fig. 4, the distance δ between the centers of the strong scatterers and that of the weak one has been varied in the range $0.335\lambda_0 \leq \delta \leq 0.808\lambda_0$ and the reconstructions have been carried out by means of both the M-IMSA and the S-IMSA. From the set of representative reconstructions shown in Fig. 10, one can observe that in the case of $\delta = 0.335\lambda_0$, the S-IMSA [Fig. 10(a)] performs better than the M-IMSA [Fig. 10(b)], since the latter is not able to detect accurately the RoI related to the weak contrast, being it in close proximity to the other scatterers. Such an inaccuracy worsens the reconstructed distribution [see Fig. 10(b) versus Fig. 10(a)] as confirmed by the estimated values of the total reconstruction error reported in Tab. I ($\xi_{tot}^{M-IMSA} \approx 1.5\xi_{tot}^{S-IMSA}$) and more significantly of the internal reconstruction error (i.e., computed only on the support of the scatterers) being $\xi_{int}^{M-IMSA} = 27.46$ versus $\xi_{int}^{S-IMSA} = 19.30$. However, it should be pointed out that such a drawback of the M-IMSA can be straightforwardly overcome by merging in an unsupervised way the RoIs when their distance is lower than $0.5\lambda_0$.

When the distance δ is increased to $0.541\lambda_0$, the effectiveness of the two strategy is quite similar even though the M-IMSA turns out to be slightly better as pictorially shown comparing Fig. 10(c) and Fig. 10(d) and quantitatively confirmed by the values of the error figures in Tab. I. Further increasing the distance between the scatterers to $\delta = 0.808\lambda_0$ the advantages of splitting the RoIs and increasing the resolution where needed are clearly pointed out in Fig. 10(e) (S-IMSA) and Fig. 10(f) (M-IMSA). While the S-IMSA strategy fails in reconstructing the weak scatterer, the morphological transformations exploited by the M-IMSA allow to correctly identify three non-connected RoIs inside the domain under test. In such a configuration, the reconstruction errors clearly highlight the efficacy of the M-IMSA in providing a reliable retrieval of the actual profiles ($\xi_{tot}^{S-IMSA} \approx 2.35\xi_{tot}^{S-IMSA}$).

The last set of experiments is aimed at evaluating the dependence of the M-IMSA performance on the dielectric characteristics of the objects under test. Referring to the original distribution of the contrast function shown in Fig. 3(a), the numerical analysis has been carried out by varying the value of the contrast of the second scatterer in the range $0.6 \leq \tau_2 \leq 1.2$, setting $\tau_1 = 1.2$. Fig. 11 shows the behavior of the total reconstruction error versus $\Delta\tau = \tau_1 - \tau_2$. As expected, the M-IMSA is more accurate than the S-IMSA and the gap is more and more evident as log as $\Delta\tau$ increases. Such results are due to the intrinsic limitation of the S-IMSA that unavoidably focuses mainly on the stronger scatterer. For completeness, some representative reconstructions concerned with such a study are then shown in Fig. 12. When $\Delta\tau = 0.0$, the reconstruction yielded with the S-IMSA [Fig. 12(a)] and that by means of the M-IMSA [Fig. 12(b)] are comparable even though the latter is slightly more accurate (see also Fig. 10). On the contrary, when $\Delta\tau = 0.4$, the dielectric distributions of the contrasts are more faithfully retrieved by the M-IMSA [Fig. 12(d)] than that through the S-IMSA [Fig. 12(c)].

IV. CONCLUSIONS

In this paper, a numerical assessment of the multiscale iterative inversion procedure that exploits a set of morphological transformations has been presented. Such an analysis has pointed out that the M-IMSA is a more robust and accurate technique for the identification of the RoIs than the standard IMSA implementation. Moreover, some indications on the robustness and current limitations of the M-IMSA versus the scatterers distances and the dielectric values of the scatterers have been drawn.

Further studies will be dedicated to analyze the class of Coordinate Logic filters [21] since they could provide a non-negligible improvement of the morphological operators. Finally, the proposed approach is expected to be less efficient when there are variations in the background as in the case of subsurface imaging problems and a suitable customization will be necessary. Such a scenario of application is currently under study.

REFERENCES

[1] J. M. Sill and E. C. Fear, "Tissue sensing adaptive radar for breast cancer detection - Experimental investigation of simple tumors models," *IEEE Trans. Microwave Theory Tech.*, vol. 53, pp. 3312-3319, Nov. 2005.

[2] Yu, T. Yu, and L. Carin, "Three-dimensional inverse scattering of a dielectric target embedded in a lossy half-space," *IEEE Trans. Geosci. Remote Sensing*, vol. 42, pp. 957-973, 2004.

[3] J. Ch. Bolomey, *Frontiers in Industrial Process Tomography*. Engineering Foundation, 1995.

[4] O. M. Bucci and G. Franceschetti, "On the degrees of freedom of scattered fields," *IEEE Trans. Antennas Propagat.*, vol. 37, pp. 918-926, July 1989.

[5] E. L. Miller and A. S. Willsky, "A multiscale, statistically based inversion scheme for linearized inverse scattering problems," *IEEE Trans. Geosci. Remote Sensing*, vol. 34, pp. 346-357, Mar. 1996.

[6] E. L. Miller, "Statistically based methods for anomaly characterization in images from observations of scattered radiation," *IEEE Trans. Image Processing*, vol. 8, pp. 92-101, Jan. 1999.

[7] E. L. Miller and A. S. Willsky, "Wavelet-based methods for nonlinear inverse scattering problem using the extended Born approximation," *Radio Sci.*, vol. 31, pp. 51-65, Jan. 1996.

[8] O. M. Bucci, L. Crocco, and T. Isernia, "An adaptive wavelet-based approach for non destructive evaluation applications," in *Proc. IEEE Antennas and Propagation Symp.*, vol. 3, pp. 1756-1759, 2000.

[9] S. Caorsi, M. Donelli, D. Franceschini, and A. Massa, "A new methodology based on an iterative multiscaling for microwave imaging," *IEEE Trans. Microwave Theory Tech.,* vol. 51, pp. 1162-1173, Apr. 2003.

[10] H. Tortel, G. Micolau, and M. Saillard, "Decomposition of the time reversal operator for electromagnetic scattering," *J. Electromagn. Waves Appl.*, vol. 13, pp. 687-719, Mar. 1999.

[11] A. Litman, D. Lesselier, and F. Santosa, "Reconstruction of two-dimensional binary obstacle by controlled evolution of a level-set ," *Inverse Problems*, vol. 14, pp. 685-706, June 1998

[12] O. M. Bucci, A. Capozzoli, and G. D'Elia, "A novel approach to scatterer localization problem," *IEEE Trans. Antennas Propagat.*, vol. 51, pp. 2079-2090, Aug. 2003.

[13] S. Caorsi, M. Donelli, and A. Massa, "Detection, location, and imaging of multiple scatterers by means of the iterative multiscaling method," *IEEE Trans. Microwave Theory Tech.*, vol. 52, pp. 1217-1228, Apr. 2004.

[14] J. Serra, *Images Analysis and Mathematical Morphology*. New York: Academic Press, 1982.

[15] A. K. Jain, *Fundamentals of Digital Image Processing*. Englewood Cliffs, NJ: Prentice-Hall, 1989.

[16] D. Colton and R. Krees, *Inverse Acoustic and Electromagnetic Scattering Theory*, Berlin, Germany: Springer-Verlag, 1992.

[17] S. Y. Semenov, A. E. Bulyshev, A. Abubakar, V. G. Posukh, Y. E. Sizov, A. E. Souvorov, P. M. van den Berg, and T. C. Williams, "Microwave-tomographic imaging of the high dielectric-contrast objects using different image-reconstruction approaches," *IEEE Trans. Microwave Theory Tech.*, vol. 53, pp. 2284-2294, Jul. 2005.

[18] S. Caorsi, A. Massa, and M. Pastorino, "A computational technique based on a real-coded genetic algorithm for microwave imaging purposes," *IEEE Trans. Geosci. Remote Sensing*, vol. 38, pp. 1697-1708, Jul. 2000.

[19] M. Donelli and A. Massa, "Computational approach based on a particle swarm optimizer for microwave imaging of two-dimensional dielectric scatterers," *IEEE Trans. Microwave Theory Tech.*, vol. 53, pp. 1761-1776, May 2005.

[20] M. Donelli, G. Franceschini, A. Martini, and A. Massa, "An integrated multi-scaling strategy based on a particle swarm algorithm for inverse scattering problems," *IEEE Trans. Geosci. Remote Sens.*, vol. 44, no. 2, pp. 298-312, Feb. 2006.

[21] B.G. Mertzios and K. Tsirikolias, "Coordinate Logic Filters and their Applications in Image Processing and Pattern Recognition," *Circuits, Systems and Signal Processing*, vol. 17, pp. 517-538, 1998.

FIGURE CAPTIONS

Figure 1. Problem Geometry.

Figure 2. The flow-chart of the M-IMSA strategy.

Figure 3. Calibration procedure. (*a*) Reference distribution of the representative test case used for calibrating the parameters μ and χ. (*b*) Results of the calibration experiments reported in terms of the total reconstruction error.

Figure 4. Original distribution of the reference profile.

Figure 5. Three homogeneous scatterers. (*a*) Reconstructed profile with SNR=20dB at the first step (s=1) of the M-IMSA and (*b*) result of the RoIs definition process.

Figure 6. Three homogeneous scatterers. Reconstructed profile by means of the M-IMSA with SNR=20dB when (*a*) s=2 and (*b*) s=3.

Figure 7. Three homogeneous scatterers. Reconstructed profile by means of the IMSA with SNR=20dB at the convergence step (*b*) s=3.

Figure 8. Three homogeneous scatterers. Image of the object function obtained by the IMSA at s=1 after thresholding.

Figure 9. Three homogeneous scatterers. Behavior of the multi-step cost function minimization for the IMSA and the M-IMSA approaches.

Figure 10. Three homogeneous scatterers. Reconstructed profile by means of (*a*) (*c*) (*e*) the IMSA and (*b*) (*d*) (*f*) the M-IMSA when (*a*) (*b*) $\delta = 0.335\lambda_0$, (*c*) (*d*) $\delta = 0.541\lambda_0$ and (*e*) (*f*) $\delta = 0.808\lambda_0$.

Figure 11. Two homogeneous scatterers. Behavior of the total reconstruction error versus the parameter $\Delta\tau = \tau_1 - \tau_2$ (SNR=20dB).

Figure 12. Two homogeneous scatterers. Reconstructed profile (SNR=20dB) by means of (*a*) (*c*) the IMSA and (*b*) (*d*) the M-IMSA when (*a*) (*b*) $\Delta\tau = 0.0$ and (*c*) (*d*) $\Delta\tau = 0.4$.

TABLE CAPTIONS

Table 1.   Three homogeneous scatterers. Values of the error figures for different scatters locations.
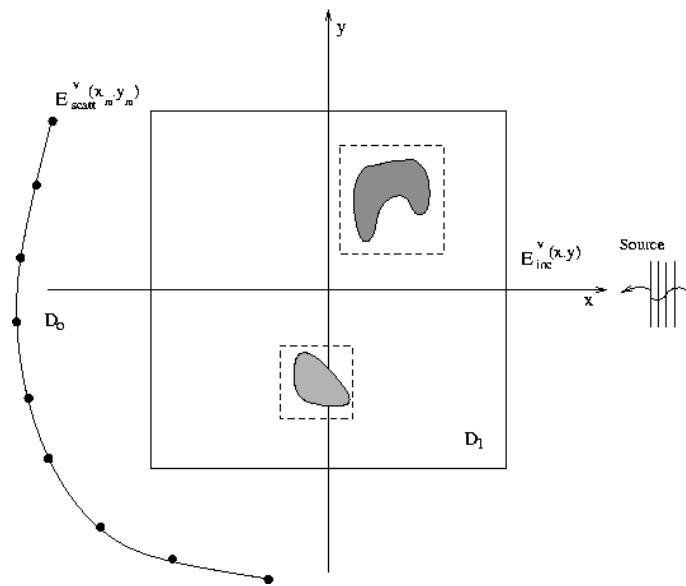
Fig. 1 – D. Franceschini *et al.*, "Morphological Processing of Electromagnetic Scattering Data…"
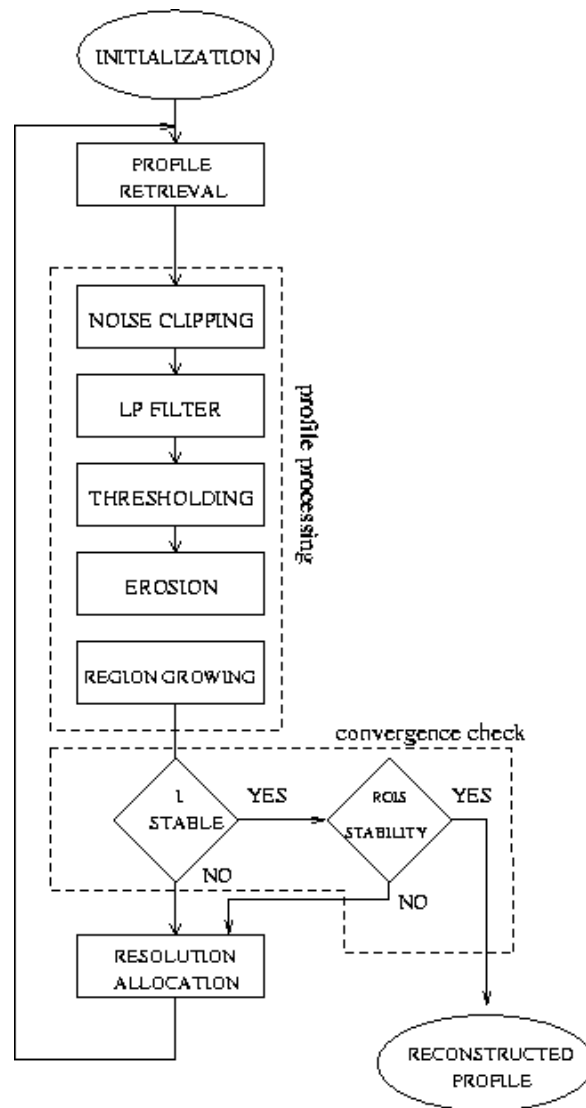
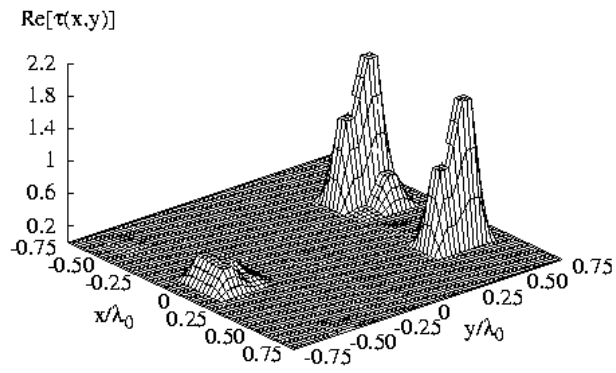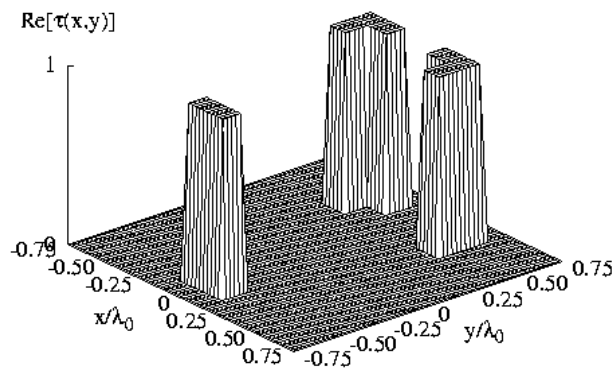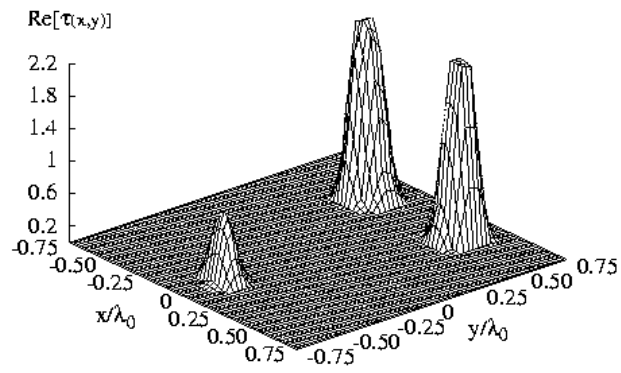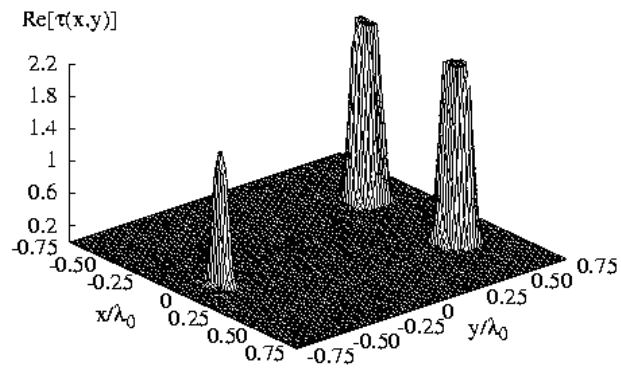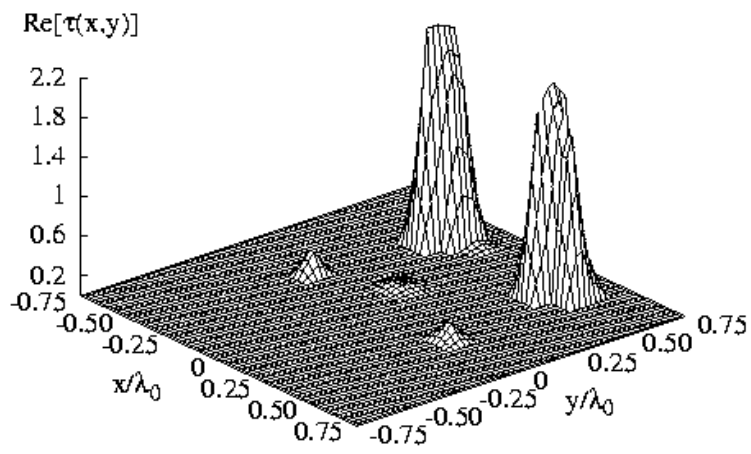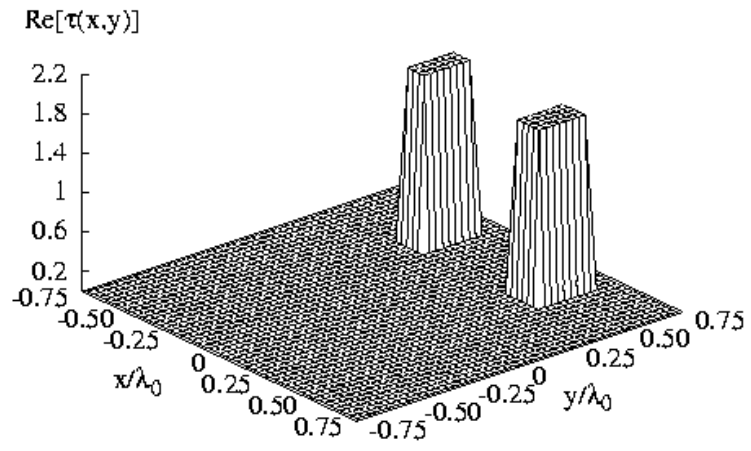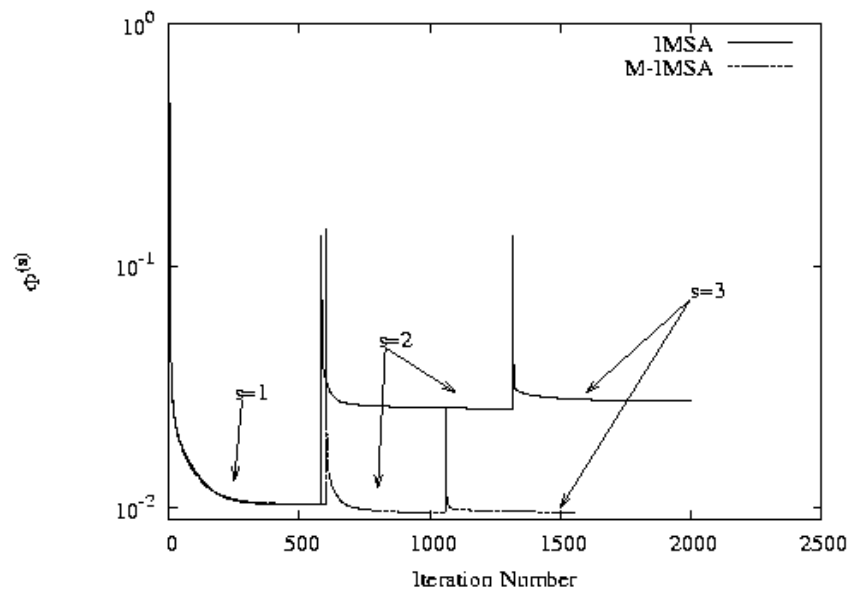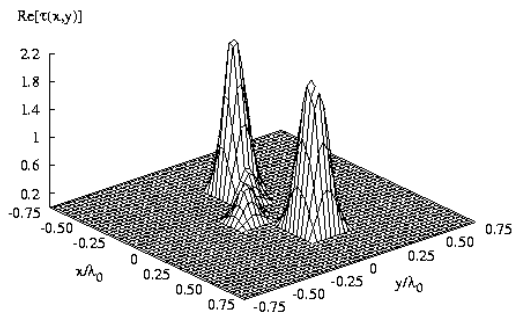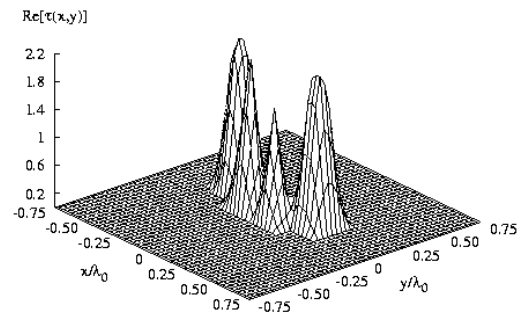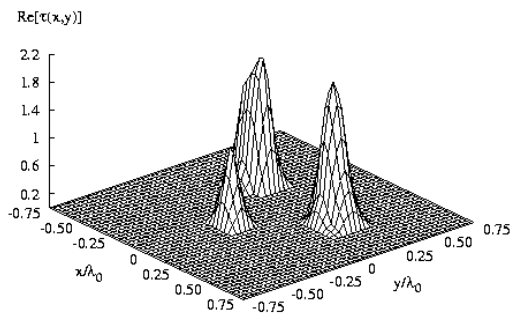**Fig. 2 – D. Franceschini** *et al.*, "Morphological Processing of Electromagnetic Scattering Data…"

Re[τ(x,y)]

(*a*)

ξ_{tot}^{M-IMSA}

(*b*)
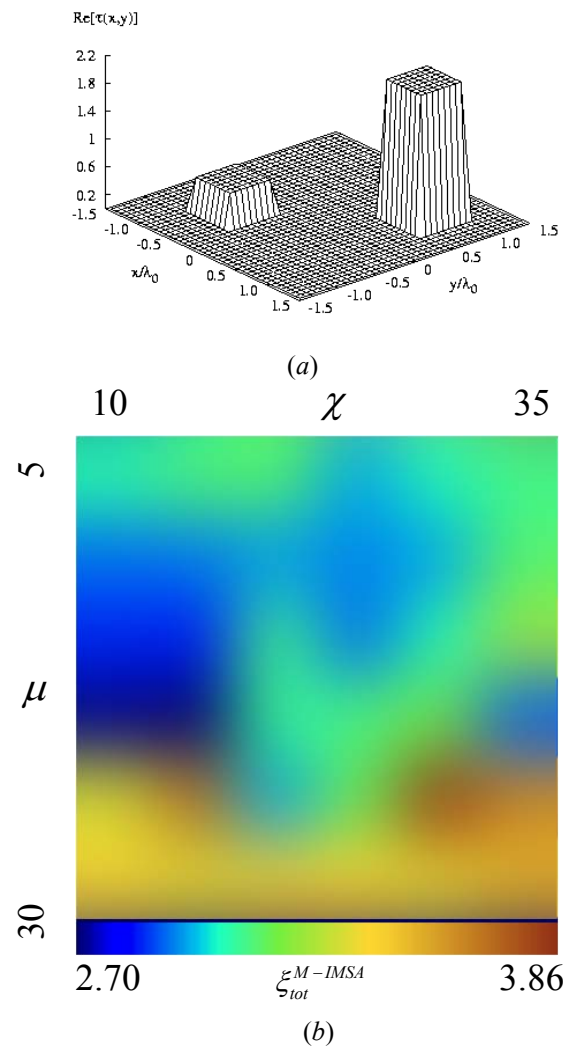
Fig. 3 – D. Franceschini *et al.*, "Morphological Processing of Electromagnetic Scattering Data…"
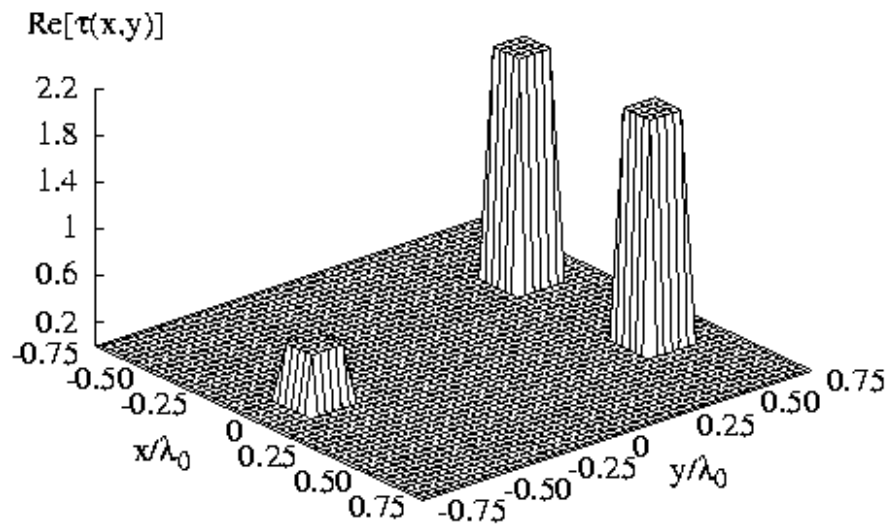
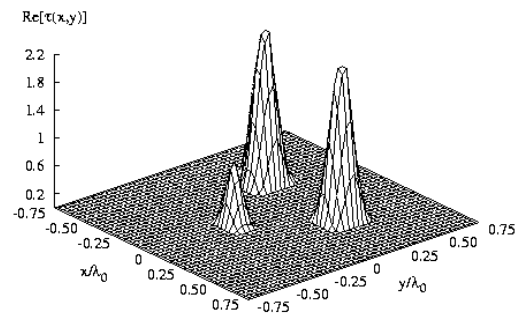Re[τ(x,y)]

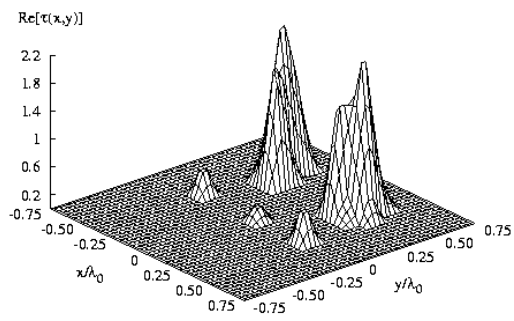**Fig. 4 – D. Franceschini** *et al.*, "Morphological Processing of Electromagnetic Scattering Data…"

Re[τ(x,y)]

2.2
1.8
1.4
1
0.6
0.2
-0.75

-0.50
-0.25
0
0.25
0.50
0.75

x/λ_0

0.75
0.50
0.25
0
-0.25
-0.50
-0.75

y/λ_0

(*a*)

Re[τ(x,y)]

1

-0.79
-0.50
-0.25
0
0.25
0.50
0.75

x/λ_0

0.75
0.50
0.25
0
-0.25
-0.50
-0.75

y/λ_0

(*b*)

Fig. 5 – D. Franceschini *et al.*, "Morphological Processing of Electromagnetic Scattering Data…"

Re[τ(x,y)]

(*a*)

Re[τ(x,y)]

(*b*)
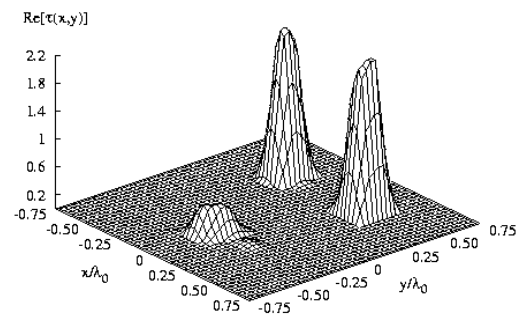
Fig. 6 – D. Franceschini *et al.*, "Morphological Processing of Electromagnetic Scattering Data…"
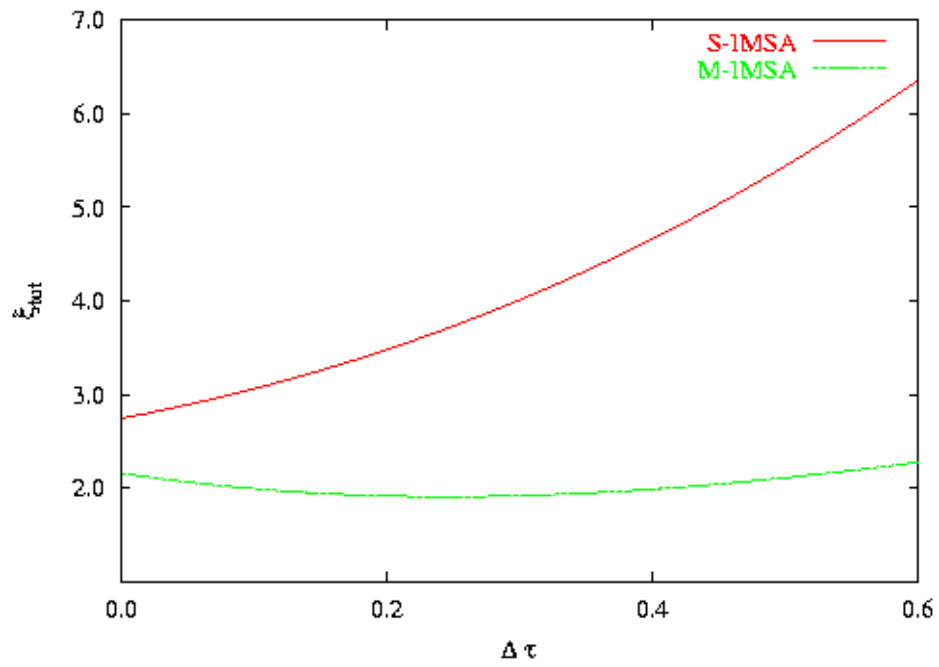
Fig. 7 – D. Franceschini *et al.*, "Morphological Processing of Electromagnetic Scattering Data…"

Re[τ(x,y)]

2.2
1.8
1.4
1
0.6
0.2
-0.75
-0.50
-0.25
0
0.25
0.50
0.75

x/λ₀

0.75
0.50
0.25
0
-0.25
-0.50
-0.75

y/λ₀

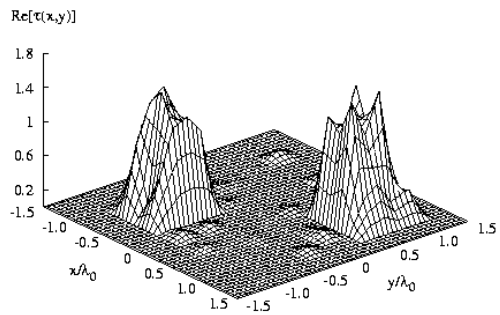**Fig. 8 – D. Franceschini** *et al.*, "Morphological Processing of Electromagnetic Scattering Data…"

Fig. 9 – D. Franceschini *et al.*, "Morphological Processing of Electromagnetic Scattering Data…"

(*a*)

(*b*)

(*c*)

(*d*)

(*e*)

(*f*)

Fig. 10 – D. Franceschini *et al.*, "Morphological Processing of Electromagnetic Scattering Data…"
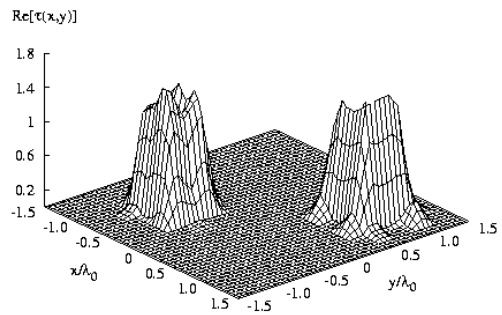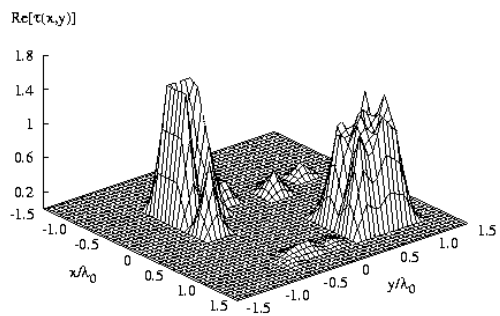
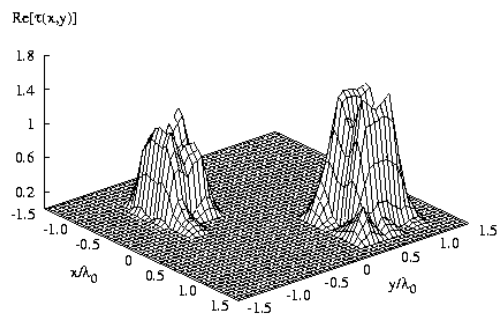**Fig. 11 – D. Franceschini** *et al.*, "Morphological Processing of Electromagnetic Scattering Data…"

(a)

(b)

(c)

(d)

Fig. 12 – D. Franceschini *et al.*, "Morphological Processing of Electromagnetic Scattering Data…"

	δ/λ_0		
	0.335	0.541	0.808
ξ_{tot}^{S-IMSA}	1.79	1.82	2.86
ξ_{tot}^{M-IMSA}	2.66	1.07	1.61
ξ_{int}^{S-IMSA}	19.30	29.12	28.50
ξ_{int}^{M-IMSA}	27.46	25.10	12.14
ξ_{ext}^{S-IMSA}	1.25	0.90	2.19
ξ_{ext}^{M-IMSA}	1.90	0.30	1.30

Tab. I – D. Franceschini *et al.*, "Morphological Processing of Electromagnetic Scattering Data…"